



# Sr-rich chromium ferrites as symmetrical solid oxide fuel cell electrodes

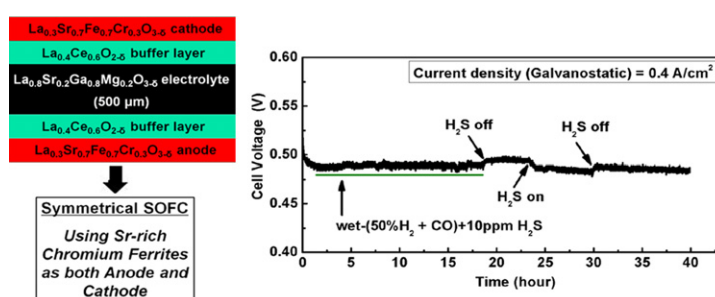
Min Chen, Scott Paulson, Venkataraman Thangadurai, Viola Birss\*

Department of Chemistry, University of Calgary, Calgary, AB T2N 1N4, Canada

## HIGHLIGHTS

- Cr-containing cathode shows  $R_p$  of  $0.1 \Omega \text{ cm}^2$  in air at  $800^\circ\text{C}$ .
- Sr-rich Ferrite shows far more better anode performance than La-rich Ferrite.
- Structural stability limit of LSFC-3 is down to a  $p\text{O}_2$  of  $1.9 \times 10^{-21} \text{ atm}$  at  $800^\circ\text{C}$ .
- $\text{LSFC-3}^{\text{wet-H}_2} \rightarrow \text{LaSrFeO}_4\text{-based phase} + \alpha\text{-Fe} \xrightarrow{\text{air}} \text{LSFC-3}$ , regenerative crystal structure.
- LSFC-3 anode performs well in wet 1:1  $\text{H}_2\text{:CO}$  fuels with  $p\text{O}_2 > 1.9 \times 10^{-21} \text{ atm}$ .

## GRAPHICAL ABSTRACT



## ARTICLE INFO

### Article history:

Received 19 December 2012

Received in revised form

1 February 2013

Accepted 12 February 2013

Available online 20 February 2013

### Keywords:

Symmetrical solid oxide fuel cell

Sulfur tolerance oxide anodes

Fe-based perovskite

In-situ X-ray diffraction

Structural stability

## ABSTRACT

For the first time, anodes and cathodes composed of  $\text{La}_{0.3}\text{Sr}_{0.7}\text{Fe}_{1-x}\text{Cr}_x\text{O}_{3-\delta}$  (LSFC,  $x = 0-0.3$ ) are used within a symmetrical solid oxide fuel cell (SSOFC).  $\text{La}_{0.8}\text{Sr}_{0.2}\text{Ga}_{0.8}\text{Mg}_{0.2}\text{O}_{3-\delta}$  (LSGM) electrolyte-supported half cells, employing  $\text{La}_{0.3}\text{Sr}_{0.7}\text{Fe}_{0.7}\text{Cr}_{0.3}\text{O}_{3-\delta}$  (LSFC-3) at both electrodes, produced electrode polarization resistances of  $0.1 \Omega \text{ cm}^2$  in air and  $0.4 \Omega \text{ cm}^2$  in wet (ca. 3%  $\text{H}_2\text{O}$ )  $\text{H}_2$  at  $800^\circ\text{C}$ . Although LSFC is robust under typical SSOFC conditions at  $500^\circ\text{C}$ , *in-situ* X-ray diffraction studies at  $800^\circ\text{C}$  in reducing atmospheres show that its perovskite structure can undergo a slow,  $p\text{O}_2$ -dependent structural change, forming a  $\text{LaSrFeO}_4$ -based Ruddlesden-Popper phase plus  $\alpha\text{-Fe}$ , a process which can be reversed in air at  $800^\circ\text{C}$ . For LSFC-3, this phase change occurs when the  $p\text{O}_2$  of the fuel is lower than  $1.9 \times 10^{-21} \text{ atm}$ . This results in an initial power drop of ca. 30% for LSFC-3-based SSOFCs when using wet  $\text{H}_2$ , but the new anode composition still maintains a promising  $0.2 \text{ W cm}^{-2}$  cell power density over several hundred hours of operation. Extended full cell tests also show that the LSFC-3 anode performs very well in wet 1:1  $\text{H}_2\text{:CO}$  fuels ( $p\text{O}_2 > 1.9 \times 10^{-21} \text{ atm}$ ) that contain 10 ppm  $\text{H}_2\text{S}$ , demonstrating the excellent versatility of this electrode material.

© 2013 Elsevier B.V. All rights reserved.

## 1. Introduction

Solid oxide fuel cells (SOFCs) are high efficiency energy conversion devices that also have several environmental advantages, including low to zero emission of pollutants ( $\text{SO}_x$ ,  $\text{NO}_x$  and particulates) and the generation of a clean and nearly pure stream of  $\text{CO}_2$

(no  $\text{N}_2$ ) ready for carbon capture and storage (CCS). From a cost and long-term performance perspective, there is also significant interest in developing symmetrical SOFCs (SSOFCs) using the same redox-stable materials as both the anode and cathode [1–4]. By employing identical anode and cathode compositions, the cell can be fired in a single step, hence reducing fabrication costs. Also, because conventional SOFC anodes are prone to sulfur poisoning and carbon deposition, the redox tolerance of SSOFCs allows regeneration of the anode chamber by periodic purges with steam or air, a process often employed to de-coke large-scale industrial processes [5].

\* Corresponding author. Tel.: +1 403 220 6432; fax: +1 403 289 9488.  
E-mail address: [birss@ucalgary.ca](mailto:birss@ucalgary.ca) (V. Birss).

However, a key challenge in the development of SSOFC electrode materials is that they must show stable, long-term performance, while also possessing high catalytic activity and electronic conductivity over many orders of magnitude  $pO_2$  change, from a  $pO_2$  of 0.21 atm at the cathode to a  $pO_2$  of  $10^{-22}$  atm at the anode. To date, many redox-stable oxides have been evaluated as potential electrodes for SSOFCs, classified as simple perovskites ( $ABO_{3-\delta}$ ) [6,7], fluorites ( $AO_{2-\delta}$ ) [8], and perovskite-like layered compositions, such as double-perovskite ( $A_2BO_{6-\delta}$ ) [3,9]. In terms of simple perovskites, high performance Co-based perovskites are typically not stable in the presence of fuels and therefore previous work has focused more on Mn- and Fe-based perovskites [10]. Extensive work has shown that substituting the B site Mn in perovskites with Ti and Cr can result in stable, high performance anodes [11,12]. A similar strategy was used to stabilize the Fe-based perovskite,  $La_{0.75}Sr_{0.25}Fe_{0.5}Cr_{0.5}O_{3-\delta}$ , which remains a single phase in 5%  $H_2$  at 900 °C for 120 h [13]. However, as is the case for most simple perovskites, heavy doping with early transition metals leads to a significant loss of electronic and ionic conductivity, while also lowering the catalytic activity for  $O_2$  reduction on the cathode side [14].

Compared to the low Sr simple perovskites, a high Sr content in the A-site of perovskite-like phases has produced high performance ceramics that are phase stable over a wide  $pO_2$  range [15,16].  $LaSr_2Fe_{3-y}Cr_yO_{8+\delta}$  oxides, targeted as membrane materials for the partial oxidation of natural gas, have excellent ionic and electronic conductivity at oxygen partial pressures ranging from 0.5 to  $10^{-22}$  atm [17]. Recently, Fe- and Co-based double-perovskite materials, such as  $Sr_2Fe_{1.5}Mo_{0.5}O_{6-\delta}$  have shown among the best SSOFC performances (ca.  $0.5\text{ W cm}^{-2}$ ) in  $H_2$ -air at 800 °C when employing a 0.3 mm thick  $La_{0.9}Sr_{0.1}Ga_{0.8}Mg_{0.2}O_{3-\delta}$  (LSGM) electrolyte support [3]. For example, a very low polarization resistances ( $R_p$ ) of 0.20–0.25  $\Omega\text{ cm}^2$  in  $H_2$  at 750–800 °C was reported for the  $LaSr_2Fe_2CrO_{8+\delta}$ – $Ce_{0.9}Gd_{0.1}O_{2-\delta}$  (GDC) composite anode [18]. Much of this work still remains in the initial stages and long-term testing under a variety of fuels and testing conditions must still be carried out.

In the present study, the high Sr content Fe-based  $La_{0.3}Sr_{0.7}Fe_{1-x}Cr_xO_{3-\delta}$  (LSFC) perovskite was selected for investigation, for the first time, as an SSOFC electrode. This was based on first increasing the electronic and ionic conductivity of a Fe-based perovskite by pushing its structural stability limit via heavy A-site substitution of La by Sr. At the extreme, it would then become structurally equivalent to the vacancy-ordered, perovskite-like, brownmillerite,  $LaSr_2Fe_3O_8$  [19], but the B site Fe should then become partially substituted by Cr to stabilize the orthorhombic perovskite and its associated high level of vacancy disorder [17]. This is because Cr has a strong preference to maintain 6-fold coordination with oxygen anions, which helps to avoid the formation of the vacancy-ordered iron–oxygen tetrahedra within the tunnels associated with layered perovskites [17]. Thus, Cr-doping can lead to a net increase, rather than a decrease, in ionic conductivity. At the same time, Cr substitution is known to increase the structural stability of  $La_{0.3}Sr_{0.7}FeO_{3-\delta}$  in reducing atmospheres [14].

This work explores the chemical (structural) stability, thermal expansion, electrical conductivity, and electrocatalytic properties of  $La_{0.3}Sr_{0.7}Fe_{1-x}Cr_xO_{3-\delta}$  (abbreviated as LSFC-0, LSFC-1, LSFC-2 and LSFC-3 for compositions with  $x = 0, 0.1, 0.2$  and  $0.3$ , respectively) over a wide range of  $pO_2$  values and temperatures. The trade-offs between these characteristics have led to the identification of the LSFC-3 material as the optimum composition for application as a SSOFC electrode. This material functions very well as a cathode and is also very good anode down to a  $pO_2$  of  $1.9 \times 10^{-21}$  atm. Even though the LSFC-3 material decomposes at a  $pO_2$  below this limit, the decomposition products (a  $LaSrFeO_4$ -based phase and  $\alpha$ -Fe) are also surprisingly active. Even more interestingly, reoxidation can

fully restore the single perovskite LSFC-3 starting material. It is shown that SSOFCs, based on LSFC-3 as both the anode and cathode, exhibit excellent long-term electrochemical performance under a variety of fuel conditions, including with exposure to a  $CO/H_2$  mixture containing 10 ppm  $H_2S$ .

## 2. Experimental

A glycine nitrate process was employed to prepare the LSFC powders. Reagent grade  $La(NO_3)_3 \cdot 6H_2O$ ,  $Sr(NO_3)_2$ ,  $Fe(NO_3)_3 \cdot 9H_2O$ ,  $Cr(NO_3)_3 \cdot 9H_2O$  and glycine were dissolved in deionized water using metal cation proportions that were based on the desired stoichiometry of each LSFC material. A 2:1 mol ratio of glycine to the total metal cation content was used. Stirred solutions were slowly heated on a hot plate until auto-ignition and self-sustaining combustion occurred. The ash was subsequently pulverized and pre-calcined at 1200 °C for 2 h in air (conditions under which single phases are generated). Powders were milled (high energy planetary ball mill, Pulverisette 5, Fritsch, Germany) in an isopropanol medium at a rotation speed of 300 rpm for 2 h using zirconia balls and were then divided into three parts, with one portion employed to investigate the material structural stability. The second portion of the LSFC powder was used for the thermal expansion and electrical conductivity measurements, while the third was employed in electrochemical testing.

The phase identification of the powders in air and dry 10%  $H_2 + N_2$  was carried out *in-situ* using a Bruker D8 Advance powder X-ray diffractometer (XRD) with a high temperature sample holder. Room temperature XRD examination of ex situ samples exposed to different fuel conditions at 800 °C for 72 h (the samples were quenched to room temperature in the same fuel environment as used at 800 °C) was also carried out. The oxygen content change in the specimens as a function of temperature was determined using thermogravimetric (TG) methods (Mettler Toledo Thermal Analysis, TGA/DSC1) at up to 900 °C in air. In order to achieve thermodynamic equilibrium during the reduction (heating) and the oxidation (cooling) of the oxide powders, a relatively low heating/cooling rate of  $2\text{ °C min}^{-1}$  was used for each TG run.

For the conductivity and thermal expansion coefficient measurement, LSFC powders were uniaxially pressed into disks and cylinders under a pressure of 100 MPa (10 mm in diameter and 1 mm in thickness), followed by sintering at 1300 °C for 4 h in air. The density of the specimens was determined using the Archimedes method, giving a value of around 95%. The pellets were polished using emery paper (SiC media, 600 mesh) to ensure surface flatness and were then coated with Pt paste. The electrical conductivity was measured using the dc Van der Pauw method at 300–900 °C in both air and wet (3% $H_2O$ )–(10% $H_2 + N_2$ ). The thermal expansion measurements were conducted using cylindrical specimens (5 mm diameter and 8 mm in thickness) by heating at  $5\text{ °C min}^{-1}$  between 50–900 °C in air, using a Linseis L75PT vertical dilatometer, with YSZ used as the calibration standard.

The  $La_{0.8}Sr_{0.2}Ga_{0.8}Mg_{0.2}O_{3-\delta}$  (LSGM, [fuelcellmaterials.com](http://fuelcellmaterials.com)) electrolyte powders were cold isostatically pressed into 35 mm pellets under a pressure of 100 MPa and pre-sintered at 1100 °C for 2 h in air to ensure adequate strength. Next, a  $La_{0.4}Ce_{0.6}O_{2-\delta}$  (LDC) buffer layer was coated onto both sides of the LSGM substrate using screen printing, followed by co-sintering at 1350 °C for 4 h. The thickness of the resulting dense electrolyte support was ca. 1 mm and 0.5 mm for the half cell and single cell studies, respectively, and the diameter was 28 mm. The LSFC powders were then screen printed symmetrically ( $1.0\text{ cm}^2$  area) onto both sides of the LSGM support and fired at 1100 °C for 2 h. Au paste (C 5729, Heraeus Inc. Germany) was painted on the LSFC layers at both sides of the pellet to serve as the anode and cathode current collectors. To

characterize the long-term cathode performance of the LSFC materials in an anode-supported single cell, a YSZ/Ce<sub>0.9</sub>Gd<sub>0.1</sub>O<sub>2-δ</sub> (GDC) bi-layer electrolyte membrane supported by a Ni-YSZ cermet was selected for this purpose. The details of fabrication of the anode-supported cell containing the LSFC-3 cathode layer are presented in the [Supporting information](#) (Section 1).

The cells were fixed in a FCSH-V3 cell holder (MaterialsMate, Italy) for the purpose of determining their electrochemical properties. For half cell testing, a single chamber mode was used by switching the chamber gas between air and fuel conditions. For single cell testing, a glass sealant (Type 613, Aremco Products, USA) was used to isolate the anode (fuel) and cathode (air) gases.

The cell performance was evaluated using a four-probe method at 800 °C. Impedance spectra were collected under open circuit conditions using a RMS amplitude of 50 mV in the frequency range of 0.01 Hz–60 kHz using a Solatron 1287/1255 potentiostat/galvanostat/impedance analyzer. Scanning electron microscope (SEM) images of the cells and electrode layers were acquired using a Philips/XL30 FEI ESEM. A JEOL JXA-8200 electron probe micro-analyzer (EPMA) was used to detect cation inter-diffusion at the interfaces within the SSOFCs.

### 3. Results and discussion

#### 3.1. Evaluation of LSFC oxides as SSOFC cathodes

##### 3.1.1. Oxygen loss at high temperatures

In order to first ensure that the desired phases had formed for the LSFC compositions under study here and that no impurities were present, XRD analysis was carried out, all at room temperature. A perovskite-like structure of LaSr<sub>2</sub>Fe<sub>3</sub>O<sub>8.94</sub> (JCPDS Card No. 80-1037, R-3c space group) was certified for all of the LSFC powders with Cr contents up to 0.3 (Section 2 of [Supporting information](#)).

In order to then establish the thermal stability of these oxides, thermogravimetric analysis (TGA) was carried out in air, with [Fig. 1](#) showing the relative weight loss of various LSFC compositions as a function of temperature. As shown in the inset for the LSFC-0 sample, the weight change is reversible upon heating and cooling in air, with the same behavior being observed for the other three compositions. Considering that the LSFC materials were prepared at 1200 °C in air, their structure should be stable under TGA condition. In this case, the observed weight change can be attributed to the loss of lattice oxygen (B site metal reduction) upon

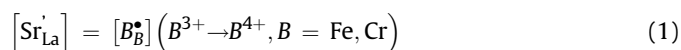
heating and the uptake of oxygen during cooling (B site metal oxidation).

In addition, it is seen that the amount of oxygen loss significantly decreases with increasing Cr content upon heating (the oxygen loss of LSFC-0, LSFC-1 and LSFC-3 at 40–900 °C is 1.58%, 1.08% and 0.61%, respectively). In this study, the LSFC materials were formed by partial substitution of Fe by Cr, which strongly prefers 6-fold coordination and thus immobilizes the lattice oxygen. Therefore, it is not surprising to observe that Cr substitution inhibits thermally-induced oxygen loss from the LSFC materials, suggesting that the LSFC-3 material would be the most stable under SSOFC conditions.

##### 3.1.2. Electrical conductivity and thermal expansion

It is critical that SSOFC electrode materials display excellent conductivity and thermal expansion coefficients that match those of the intended electrolyte. [Fig. 2](#) displays the electrical conductivity and linear thermal expansion curves (LTECs) of the LSFC specimens as a function of temperature in air. As can be seen in [Fig. 2a](#), the electrical conductivity of each specimen increases with increasing temperature up to a maximum value (designated as  $T_{max}$ ) and then decreases. This indicates a transition in electrical conduction from semiconducting to metallic, typical of perovskite-type mixed conductors, which are predominantly electronic conductors [20–22]. Consequently, the electrical conductivity measured by the dc Van der Pauw method in this study is actually the electronic conductivity [23].

In the LSFC perovskites, the A-site ions were formed by partial substitution of La by Sr. In order to maintain charge neutrality, the A-site acceptor dopant (Sr<sup>2+</sup>) is compensated electronically by the oxidation of the B site metal (B<sup>3+</sup> to B<sup>4+</sup>) or ionically by the formation of oxygen vacancies [20]. In the lower temperature range (when the oxygen content in the LSFC oxides is constant, as shown in [Fig. 1](#)), the former process would dominate the compensation, introducing p-type charge carriers in the form of small polarons, which can be expressed by Kröger–Vink notation as:



The mobility of these types of charge carriers increases with increasing temperature up to  $T_{max}$  ([Fig. 2a](#)), resulting in an increase in the electrical conductivity. However, after a further increase in the temperature, the lattice oxygen is released, as indicated in [Fig. 1](#). Electronic and ionic compensation then take place simultaneously and compete with each other. This phenomenon results in a decrease in the electrical conductivity at  $> T_{max}$ , as seen in [Fig. 2a](#), with more explanations presented in the [Supporting information](#) (Section 3).

[Fig. 2a](#) also shows that, at constant temperature, the electrical conductivity generally decreases with increasing Cr content, except for that of LSFC-3 in the temperature range of 300–350 °C. In a perovskite-type mixed conductor containing more than one type of transition metal cation, the charge carriers tend to follow pathways through the lattice that require the lowest energy, with the small-polaron site energy of the transition metal cations sorted as Mn < Cr < Fe [24]. In LSFC, Cr possesses a lower small-polaron site energy than does the Fe sites, which act as traps to temporarily immobilize the charge carriers, thereby lowering the concentration of Fe<sup>4+</sup>. In other words, the addition of the acceptor dopant (Sr<sup>2+</sup>) may be preferentially compensated for by forming Cr<sup>4+</sup> ions instead of Fe<sup>4+</sup>.

When insufficient thermal energy is available for the p-type charge carriers to overcome the energy gap between the traps and the Fe hopping sites, the electrical conductivity will decrease dramatically with an increase in the number of Cr traps, as shown

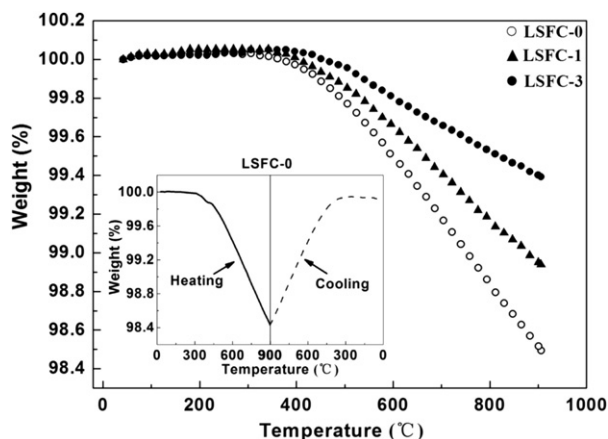


**Fig. 1.** Thermogravimetric (TG) weight loss of various La<sub>0.3</sub>Sr<sub>0.7</sub>Fe<sub>1-x</sub>Cr<sub>x</sub>O<sub>3-δ</sub> (LSFC,  $x = 0-0.3$ ) compositions as a function of temperature in air. Inset shows the TG weight change of the La<sub>0.3</sub>Sr<sub>0.7</sub>FeO<sub>3-δ</sub> (LSFC-0) sample upon heating and cooling. A relatively low heating/cooling rate of 2 °C min<sup>-1</sup> was used for each TG run.

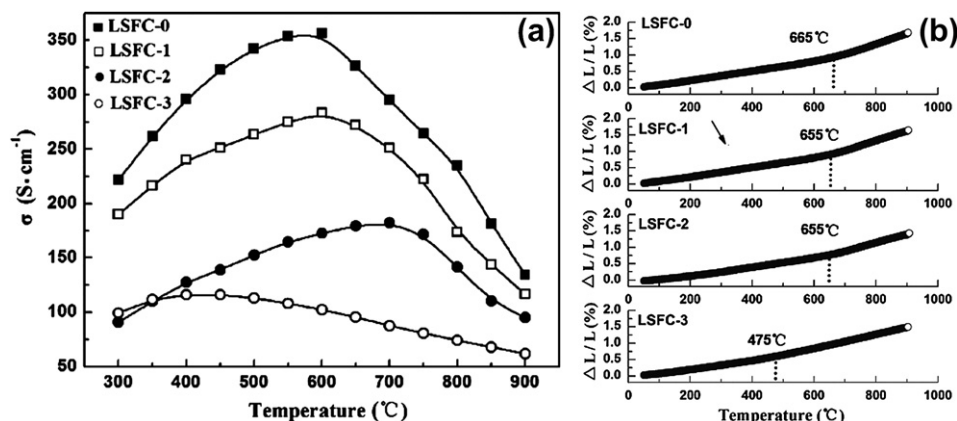


Fig. 2. (a) Electrical conductivity and (b) linear thermal expansion curves (LTECs) of the LSFC specimens as a function of temperature in air.

in Fig. 2a. This is the main reason for the negative effect of Cr substitution on the electrical conductivity of the LSFC materials. As soon as the population of the low-energy Cr sites approaches the site percolation limit (around 31%) [20], as in LSFC-3, the charges carriers are able to move through them. Therefore, compared to LSFC-2, the much higher electrical conductivity of LSFC-3 at 300–350 °C can be explained by the generation of new conducting pathways along the Cr sites. However, the mobility of the charge carriers via the Cr sites is much lower than via the Fe sites due to their poor connectivity. Thus, the measured electrical conductivity of LSFC-3, which shows the lowest electrical conductivity at 400–900 °C due to its high Cr content, remains governed by the conduction of charge carriers via the Fe sites. Even so, the electrical conductivity of the LSFC material is generally in the range of 75–225 S cm<sup>-1</sup> at 800 °C, which is superior to that of any other reported SSOFC electrodes having a perovskite structure [1].

Fig. 2b shows the thermal expansion data for the LSFC materials in air, revealing a temperature (designated as  $T_{sc}$ ), corresponding to the slope change in the linear thermal expansion curves (LTEC) in Fig. 2b for each oxide with a Cr content of 0, 0.1, 0.2 and 0.3, respectively. This behavior is similar to what has been reported previously for the  $\text{La}_{1-x}\text{Sr}_x\text{Co}_{1-y}\text{Fe}_y\text{O}_{3-\delta}$  perovskites, explained by a chemically-induced lattice expansion caused by oxygen loss and the formation of oxygen vacancies, along with Fe or Cr reduction, at high temperatures [25]. Therefore, the thermal expansion coefficients (TEC) in Fig. 2b were calculated separately over the low (50 °C –  $T_{sc}$ ) and high ( $T_{sc}$  – 900 °C) temperature ranges, as well as over the full temperature range.

Table 1 (and Fig. 2b) clearly show that Cr plays a very positive role in decreasing the TEC values of the LSFC materials, bringing them closer to the TEC values for typical SOFC electrolytes, such as YSZ ( $10.9 \times 10^{-6} \text{ K}^{-1}$ ), CGO ( $\text{Ce}_{0.8}\text{Gd}_{0.2}\text{O}_{1.9}$ ,  $12.7 \times 10^{-6} \text{ K}^{-1}$ ) and

LSGM ( $11.3 \times 10^{-6} \text{ K}^{-1}$ ) at 30–1000 °C [26]. This is because Cr suppresses the oxygen loss from the LSFC materials (Fig. 1). Importantly, compared to the very well known cathode material  $\text{La}_{0.6}\text{Sr}_{0.4}\text{Co}_{0.2}\text{Fe}_{0.8}\text{O}_{3-\delta}$  (LSCF) [27], LSFC-3, in particular, shows superior TEC values, especially in the high temperature range of 700–900 °C (most reported SSOFCs operate in this temperature range [1]).

It is clear that the maximum in Fig. 2a and the slope change in Fig. 2b arise from the thermally-induced oxygen loss. However, it was found in this work that  $T_{max}$  (Fig. 2a),  $T_{sc}$  (temperature corresponding to the slope change in the LTEC in Fig. 2b), and  $T_{ol}$  (onset temperature of oxygen loss in the TGA experiments) can vary, even for the same LSFC composition. This has been ascribed to the effect of the test conditions on the state (equilibrium or non-equilibrium) of lattice oxygen in the samples, with more detail presented in the Supporting information (Section 4).

### 3.1.3. Electrochemical performance under cathode conditions (half cell)

The activity of the LSFC materials toward the oxygen reduction reaction (ORR) was determined by measuring the impedance of symmetrical half cells in air at 800 °C. Fig. 3 shows the impedance spectra of the 2-electrode LSFC-based symmetrical half cells measured at 800 °C at the open circuit potential (OCP). The half cells consisted of a 1 mm thick  $\text{La}_{0.8}\text{Sr}_{0.2}\text{Ga}_{0.8}\text{Mg}_{0.2}\text{O}_{3-\delta}$  (LSGM)

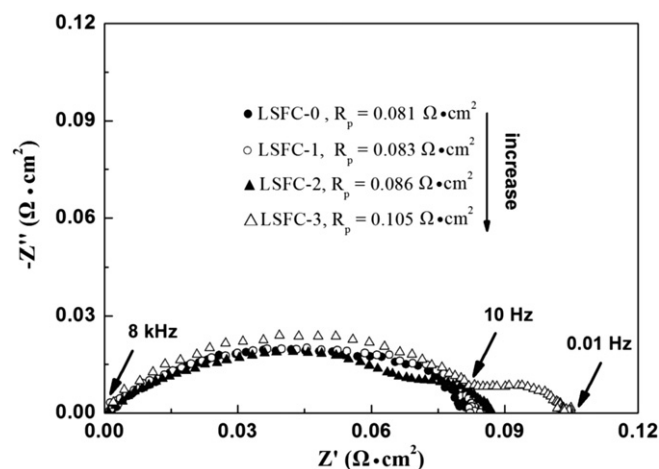


Fig. 3. Impedance spectra of the LSFC-based symmetrical half cells measured in air at 800 °C at the open circuit potential (OCP). The ohmic resistance ( $R_s$ ) was removed from the impedance data and the intercept of the impedance arcs with the real axis at low frequencies corresponds to the polarization resistance ( $R_p$ ).

**Table 1**  
Average thermal expansion coefficients over various temperature ranges for LSFC materials with varying Cr content.

Compositions <sup>a</sup>	Average TEC ( $\times 10^{-6} \text{ K}^{-1}$ )		
	Full temperature range	Low temperature range	High temperature range
LSFC-0	19.2 (50–900 °C)	14.8 (50–665 °C)	30.4 (665–900 °C)
LSFC-1	18.7 (50–900 °C)	14.5 (50–655 °C)	28.9 (655–900 °C)
LSFC-2	17.5 (50–900 °C)	13.3 (50–655 °C)	25.0 (655–900 °C)
LSFC-3	16.3 (50–900 °C)	13.5 (50–475 °C)	20.9 (475–900 °C)
LSCF <sup>b</sup> [26]	16.8 (100–900 °C)	14.9 (100–700 °C)	23.6 (700–900 °C)

<sup>a</sup>  $\text{La}_{0.8}\text{Sr}_{0.2}\text{Fe}_{1-x}\text{Cr}_x\text{O}_{3-\delta}$  is abbreviated as LSFC-0, LSFC-1, LSFC-2 and LSFC-3 for composition with  $x = 0, 0.1, 0.2$  and  $0.3$ , respectively.

<sup>b</sup> LSCF represents  $\text{La}_{0.6}\text{Sr}_{0.4}\text{Co}_{0.2}\text{Fe}_{0.8}\text{O}_{3-\delta}$ .

support, coated on both sides with a 10  $\mu\text{m}$   $\text{La}_{0.4}\text{Ce}_{0.6}\text{O}_{2-\delta}$  (LDC) buffer layer and then a 10  $\mu\text{m}$  LSFC electrode layer with an area of 1  $\text{cm}^2$  (Section 5 of Supporting information).

In order to more clearly demonstrate the variation of polarization resistance ( $R_p$ ), which is inversely proportional to the ORR activity, as a function of Cr content, the ohmic resistance ( $R_s$ ) was removed from the impedance data in Fig. 3. As can be seen, the  $R_p$  values are quite small, increasing from 0.081 to 0.105  $\Omega\text{cm}^2$  with increasing Cr content. Notably, these values are superior to what has been reported for the very well known cathode material LSCF (0.18  $\Omega\text{cm}^2$  at 800  $^\circ\text{C}$ ) [27,28]. This promising catalytic activity for the ORR can be attributed, at least in part, to the excellent ionic and electronic conductivity of the LSFC materials, which arises from A-site substitution of La by a high content of Sr. The very good performance shown in Fig. 3 is likely also related to the small grain size of the LSFC electrodes (around 500 nm, as shown in Section 5 of Supporting information), providing a high surface area for the oxygen reduction reaction.

### 3.1.4. Summary of effect of Cr content on properties and performance of LSFC in air

Based on the above results, it clear that Cr substitution results in a decrease in the electrical conductivity of  $\text{La}_{0.3}\text{Sr}_{0.7}\text{FeO}_{3-\delta}$  (Fig. 2a). Even so, the LSFC-3 specimen still exhibits an excellent electrical conductivity of 75  $\text{S cm}^{-1}$  at 800  $^\circ\text{C}$ , which is almost within the range of the required electrical conductivity for a conventional SOFC cathode [29]. While Cr greatly decreases the TEC, thus improving its compatibility with the SOFC electrolytes, an increasing Cr content does have a small negative effect on the electrochemical activity toward oxygen reduction. Taking all of these factors into consideration, including the good physical stability (thermal expansion properties) and electrochemical activity, LSFC-3 is considered as a very promising cathode for SSOFC applications.

### 3.1.5. Performance of LSFC-3 cathode in a Ni-YSZ supported cell

In order to characterize the cathode performance under more practical conditions, an LSFC-3 cathode layer, with a thickness of approximately 25  $\mu\text{m}$  and an area of 1  $\text{cm}^2$ , was deposited on a YSZ (15  $\mu\text{m}$ )/GDC (15  $\mu\text{m}$ ) bi-layer electrolyte membrane, supported by a 1 mm Ni-YSZ cermet with a porosity of 40% (Section 5 of Supporting information). The performance of the resulting anode-supported cell

at 800  $^\circ\text{C}$  with 3% $\text{H}_2\text{O}$ – $\text{H}_2$ /air is displayed in Fig. 4. It can be seen that the cell exhibits a maximum power density of 0.63  $\text{W cm}^{-2}$  (inset A of Fig. 4), which is comparable to that of LSCF cathode-based cells in a similar anode-supported configuration [27]. More importantly, in the galvanostatic mode at 0.75  $\text{A cm}^{-2}$ , a fairly low degradation rate of 0.13  $\text{mV h}^{-1}$  is seen over 100 h, demonstrating good long-term stability of the LSFC-3 cathode under typical operating conditions.

Considering that Au paste was painted on the surface of the cathode as the current collector, the gradual sintering of the Au at 800  $^\circ\text{C}$  may slow down air diffusion into the cathode layer, contributing to the slight degradation in the cell performance (Fig. 4). This assumption is also supported by the cell impedance spectrum (inset B of Fig. 4), in which the  $R_p$  values, especially the low frequency arc (often suggested to arise from gas transport limitations), shows a more significant increase than the  $R_s$  values after the long-term test. Based on the results in Fig. 4, the LSFC-3 material is clearly a very promising and stable cathode material for SSOFC applications.

### 3.2. Evaluation of LSFC as a SSOFC anode

#### 3.2.1. Short-term structural stability in dry-(10% $\text{H}_2 + \text{N}_2$ )

As is generally recognized, one of the primary requirements of SOFC anodes is their structural stability under varying fuel conditions. Fig. 5 shows the *in-situ* XRD patterns of the LSFC materials at various temperatures in dry-(10% $\text{H}_2 + \text{N}_2$ ). Data for each pattern were acquired over a 2 h period, with the acquisition sequence for each sample shown in Fig. 5 from bottom to top. The brownmillerite (layered perovskite) structure for LSFC-0 is observed at 500  $^\circ\text{C}$  due to the formation of ordered oxygen vacancies, but this does not appear in the XRD patterns of the other samples, implying that the long-range oxygen vacancy distribution in the Cr-containing LSFC materials remains disordered. At 800 and 900  $^\circ\text{C}$  in the dry-(10% $\text{H}_2 + \text{N}_2$ ) environment, LSFC-0, LSFC-1 and LSFC-2 all show phase conversion, whereas LSFC-3 shows remarkably good structural stability, with all of the major peaks still assigned to the perovskite phase at 900  $^\circ\text{C}$ . These results show the important contribution of Cr substitution in improving the structural stability of the LSFC materials in low  $\text{pO}_2$  environments and also provide another reason to use LSFC-3 as an electrode material for SSOFCs. Consequently, the anode studies discussed in the following sections focus only on LSFC-3.

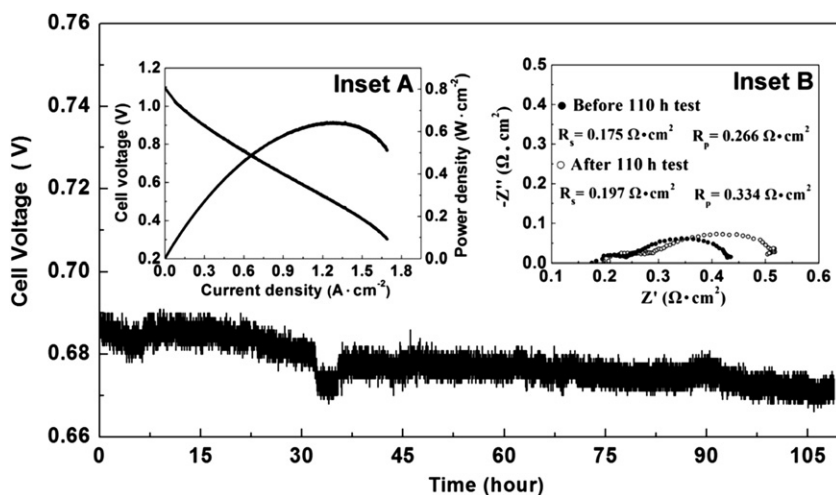
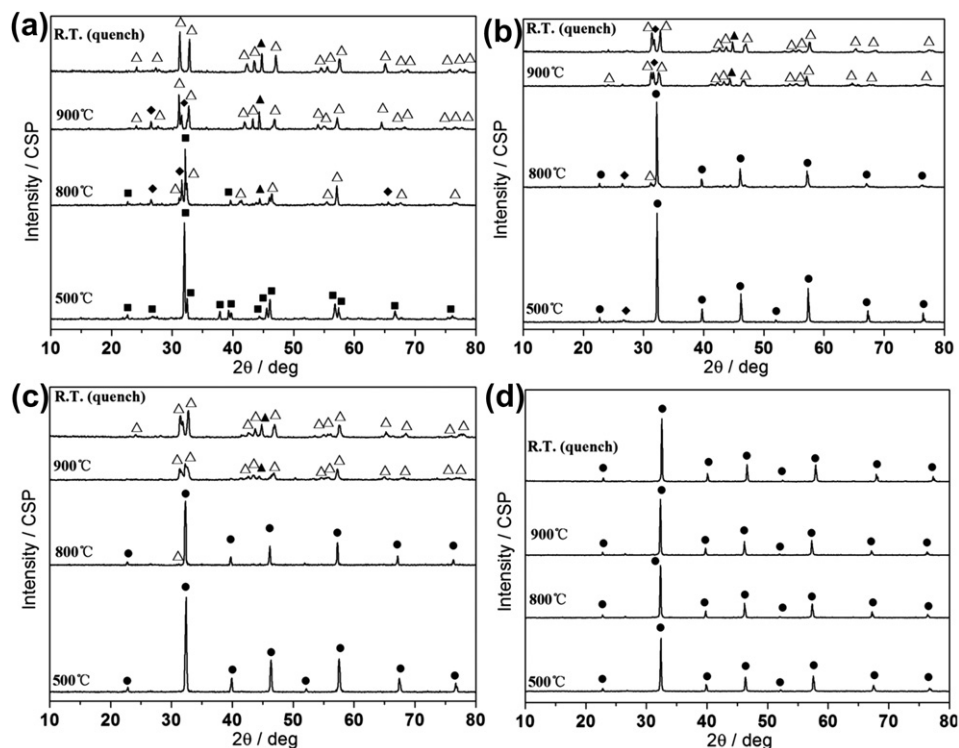


Fig. 4. Performance of the LSFC-3 material as a cathode in a Ni-YSZ anode-supported cell, measured at 800  $^\circ\text{C}$  with wet- $\text{H}_2$  as the fuel and air as the oxidant. The galvanostatic measurement was conducted at 0.75  $\text{A cm}^{-2}$  for 110 h. Inset A shows the potential and power density plots, obtained at a scan rate of 1  $\text{mV h}^{-1}$  before the galvanostatic measurement. Impedance spectra collected before and after the galvanostatic measurements are displayed in inset B.



**Fig. 5.** Short-term *in-situ* XRD patterns of the LSFC materials at various temperatures in dry-(10% $H_2 + N_2$ ) for (a) LSFC-0, (b) LSFC-1, (c) LSFC-2 and (d) LSFC-3. Each pattern was scanned for 2 h. The symbols used to identify the peaks are as follows: (●) LSFC-3 (perovskite); (■)  $LaSr_2Fe_3O_8$  (brownmillerite); ( $\Delta$ )  $LaSrFeO_4$ -based phase ( $K_2NiF_4$ ); (◆)  $La_2SrFe_2O_7$ -based phase; and (▲)  $\alpha$ -Fe.

### 3.2.2. Long-term structural stability of LSFC-3 in dry-(10% $H_2 + N_2$ ) at 800 °C

Long-term, *in-situ* high temperature reduction studies were performed in order to determine whether the phase stability of the LSFC-3 perovskite seen in Fig. 5d can be maintained over longer periods of time, and if not, which conditions would lead to a reversible interconversion between phases. Fig. 6a shows the

evolution of the *in-situ* XRD pattern of the LSFC-3 powder in dry-(10% $H_2 + N_2$ ) with time at 800 °C in the  $2\theta$  range of 30–50°. The perovskite structure of LSFC-3 persists for 4 h, but after 10 h, new phases are observed. Longer times lead to the gradual conversion to a  $LaSrFeO_4$ -based phase ( $K_2NiF_4$ -like Ruddlesden–Popper phase) and  $\alpha$ -Fe. An exact assignment of the chemical stoichiometry of this new phase could not be made using the XRD data. However, a

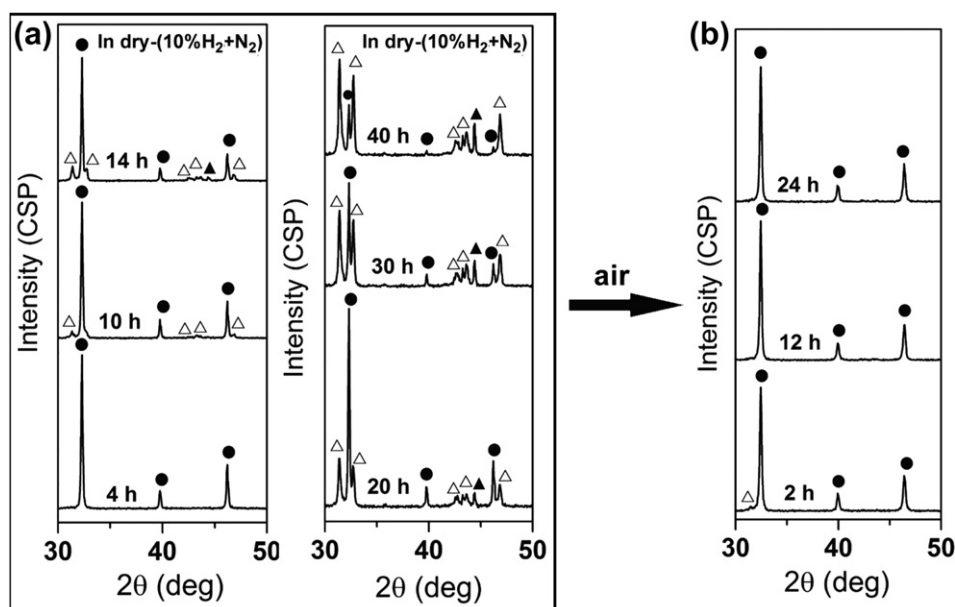
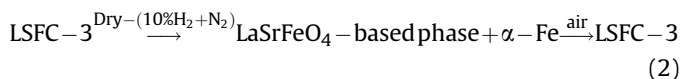


**Fig. 6.** *In-situ* XRD patterns of the LSFC-3 material (a) in dry-(10% $H_2 + N_2$ ) with time, followed by (b) introduction of air for 24 h at 800 °C in the  $2\theta$  ranges of 30–50°. The symbols used to identify the peaks are as follows: (●) LSFC-3 (perovskite); ( $\Delta$ )  $LaSrFeO_4$ -based phase ( $K_2NiF_4$ ); and (▲)  $\alpha$ -Fe.

similar product has been observed in the literature during the deposition of thin films by pulsed laser deposition using a  $\text{La}_{0.5}\text{Sr}_{0.5}\text{FeO}_3$  target [30]. The presence of  $\alpha\text{-Fe}$  has also been reported in literature [31]. Thus, the role of Cr in preserving the phase stability of LSFC-3 at 800 °C in dry-(10% $\text{H}_2 + \text{N}_2$ ) (Fig. 5d) seems to be based on a kinetic rather than thermodynamic argument. However, it is surprising to observe how rapidly the original LSFC-3 perovskite phase can be regenerated at 800 °C simply by replacing the dry-(10% $\text{H}_2 + \text{N}_2$ ) gas with air (Fig. 6b). This result shows the excellent regenerative capability of LSFC-3, with the entire process at 800 °C being expressed as:



The interconversion of segregated  $\alpha\text{-Fe}$  and Fe cations fully incorporated into a single perovskite phase has not been reported previously in the literature. The current understanding is that  $\alpha\text{-Fe}$  can be reversibly formed and rein-corporated, as long as the  $\alpha\text{-Fe}$  nanoparticles are not allowed to become too large. However, the XRD technique, employed in Fig. 6, is not sensitive enough to verify this assumption. Therefore, the effect of the size and shape of the  $\alpha\text{-Fe}$  particles on the regeneration of LSFC-3 will be the subject of our future work.

### 3.2.3. Structural stability limit of LSFC-3 at 800 °C

Because the anode compartment of an SOFC is never fully dry (water is present in the fuel or is generated by the operating cell), the  $p\text{O}_2$  level in the anode compartment can vary by many orders of magnitude. At high  $p\text{O}_2$ , this should provide structural stability to the LSFC-3 anode. Thus, a more comprehensive study was performed to determine the relationship between  $p\text{O}_2$  and LSFC-3 phase stability. In this work, powder samples were exposed to a reducing atmosphere with varying levels of  $p\text{O}_2$  at 800 °C for 72 h. The  $p\text{O}_2$  values were adjusted by systematically changing the  $\text{H}_2/\text{N}_2$  ratio in wet (ca. 3% $\text{H}_2\text{O}$ )-( $\text{H}_2 + \text{N}_2$ ) mixtures. As water vapor may react with the Be window in the sample holder of the *in-situ* XRD instrument, only room temperature XRD studies could be performed on quenched samples.

Fig. 7a shows a comparison between the *ex situ* XRD patterns of samples exposed to wet- $\text{H}_2$  ( $\log[p\text{O}_2] = -21.5$ ), wet-(10% $\text{H}_2 + \text{N}_2$ ) ( $\log[p\text{O}_2] = -19.4$ ), and dry-(10% $\text{H}_2 + \text{N}_2$ ) ( $\log[p\text{O}_2] = -23$ ) (the  $p\text{O}_2$  values were measured *in-situ* using an oxygen sensor). The LSFC-3 powder undergoes a phase conversion in both wet- $\text{H}_2$  and dry-(10% $\text{H}_2 + \text{N}_2$ ), but is found to be stable in wet-(10% $\text{H}_2 + \text{N}_2$ ). The  $p\text{O}_2$  stability range for the LSFC-3 perovskite phase was further refined in Fig. 7b, which shows the XRD patterns of three LSFC-3 powders exposed at 800 °C for 72 h to wet-(80% $\text{H}_2 + \text{N}_2$ ) ( $\log[p\text{O}_2] = -21.3$ ), wet-(70% $\text{H}_2 + \text{N}_2$ ) ( $\log[p\text{O}_2] = -21.0$ ), and wet-(60% $\text{H}_2 + \text{N}_2$ ) ( $\log[p\text{O}_2] = -20.4$ ). When the  $\text{H}_2$  content is  $\geq 70\%$ , the  $\text{LaSrFeO}_4$ -based phase is present, indicating that the structural stability limit of LSFC-3 is at the  $p\text{O}_2$  of wet-(60% $\text{H}_2 + \text{N}_2$ ), i.e., at a  $p\text{O}_2$  of ca.  $1.9 \times 10^{-21}$  atm. This is shown graphically in Fig. 7c. Although an *ex situ* XRD study was not performed on LSFC-3 exposed to wet-(50% $\text{H}_2 + \text{CO}$ ), the open circle in Fig. 7c was added to indicate the potential stability range of LSFC-3 in wet-(50% $\text{H}_2 + \text{CO}$ ), a simulated syngas reformat that is explored further below.

### 3.2.4. Electrochemical performance of LSFC-3 under anode conditions (half cell)

Half cell studies were employed to understand how the  $\text{H}_2$ -induced phase change of LSFC-3 might impact on the anode performance. Fig. 8 shows the long-term monitoring (up to 96 h) of 2-

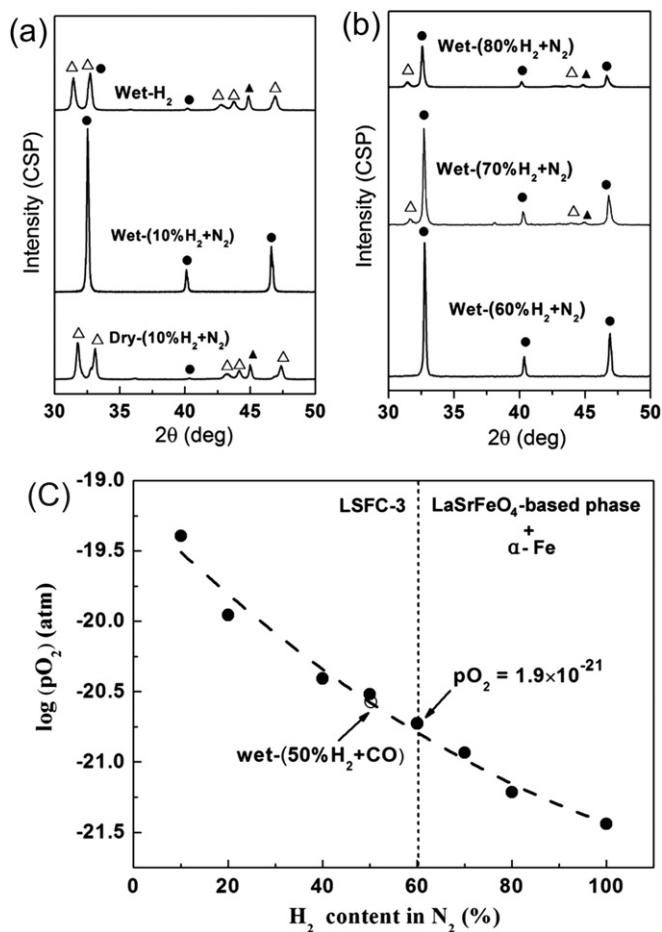
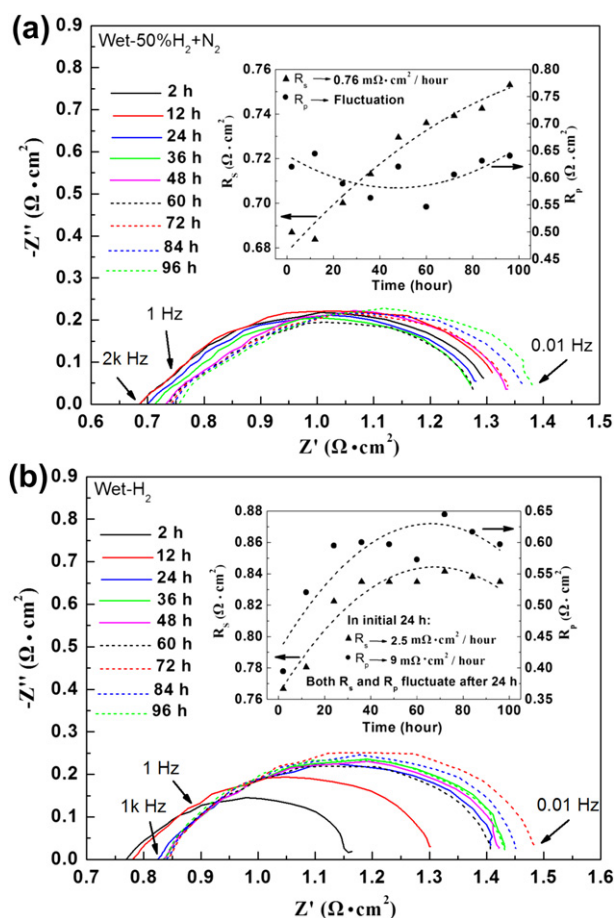


Fig. 7. *Ex situ* XRD patterns of the LSFC-3 material exposed to various wet-( $\text{H}_2 + \text{N}_2$ ) mixtures at 800 °C for 72 h, including (a) dry-(10% $\text{H}_2 + \text{N}_2$ ), wet-(10% $\text{H}_2 + \text{N}_2$ ), wet- $\text{H}_2$  and (b) wet-(60–80% $\text{H}_2 + \text{N}_2$ ). The symbols used to identify the peaks are as follows: (●) LSFC-3 (perovskite); (Δ)  $\text{LaSrFeO}_4$ -based phase ( $\text{K}_2\text{NiF}_4$ ); and (▲)  $\alpha\text{-Fe}$ . The corresponding  $p\text{O}_2$  of the wet-( $\text{H}_2 + \text{N}_2$ ) mixtures is plotted in (c) vs. the  $\text{H}_2$  content. On the left of the dashed vertical line is the region of stability of LSFC-3, while the right side corresponds to the region of stability of the reduced products, the  $\text{LaSrFeO}_4$ -based phase and  $\alpha\text{-Fe}$ .

electrode impedance data of two LSFC-3-based symmetrical half cells at 800 °C in both wet-(50% $\text{H}_2 + \text{N}_2$ ) (Fig. 8a) and wet- $\text{H}_2$  (Fig. 8b) fuel environments. At the higher  $p\text{O}_2$  level of wet-(50% $\text{H}_2 + \text{N}_2$ ), conditions under which the LSFC-3 perovskite phase was found to be stable (Fig. 7), the impedance data are very promising. The  $R_p$  value is quite low, being only ca.  $0.60 \Omega \text{ cm}^2$ , and it also remains very stable over 96 h of testing (see Fig. 8a, inset). While there is a slow increase ( $0.76 \text{ m}\Omega \text{ cm}^2 \text{ h}^{-1}$ ) seen in  $R_s$  (Fig. 8a, inset), this is likely due to other long-term cell degradation issues at 800 °C, and not the LSFC-3 electrodes.

At the lower  $p\text{O}_2$  level (Fig. 8b), conditions under which LSFC-3 should slowly convert to the new phases (Fig. 7), the initial impedance response in wet- $\text{H}_2$  exhibits a very promising  $R_p$  value of  $0.40 \Omega \text{ cm}^2$ , comparable to what has been reported for some of the best  $\text{Sr}_{1.5}\text{Fe}_{1.5}\text{MoO}_{6-\delta}$  electrodes being investigated for SSOFC applications at 800 °C [3], and much better than what is obtained with La-rich,  $\text{La}_{0.75}\text{Sr}_{0.25}\text{Cr}_{0.5}\text{Fe}_{0.5}\text{O}_{3-\delta}$  anodes [13]. However,  $R_p$  increases by ca. 30% over roughly the same 30–40 h time period in which the LSFC-3 phase change was seen to occur by XRD (Fig. 6a), although it stabilizes at a still low  $0.60 \Omega \text{ cm}^2$  (Fig. 8b, inset).  $R_s$  increases at a similar rate in both gas compositions (Fig. 8a and b), but also stabilizes in the wet- $\text{H}_2$  environment.



**Fig. 8.** Long-term monitoring (up to 96 h) of the 2-electrode impedance spectra of two LSCF-3-based symmetrical half cells at 800 °C in (a) wet-(50%H<sub>2</sub> + N<sub>2</sub>) and (b) wet-H<sub>2</sub>. The change in both  $R_p$  and  $R_s$  with time is displayed in the insets.

In summary, although the LSCF-3 perovskite phase undergoes a significant phase change under extreme SSOFC anode reducing conditions, its performance still remains very good. While it is not known what the precise cause of the  $R_p$  loss during the LSCF-3 phase change in wet-H<sub>2</sub> may be, an important advantage is that the electrical conductivity of LSCF-3 is 0.25 S cm<sup>-1</sup> at 800 °C in wet-(10%H<sub>2</sub> + N<sub>2</sub>) (Section 6 of Supporting information), which is almost 7 times higher than that of the LaSrFeO<sub>4</sub>-based phase.

### 3.3. Performance of LSCF-3-based SSOFCs

LSGM electrolyte-supported full cell studies, using LSCF-3 as both the anode and cathode, were carried out to assess the SSOFC performance in a variety of fuel compositions. Fig. 9 shows a long-term cell voltage vs. time plot (Fig. 9a) and the power curves (Fig. 9b) of the LSCF-3-based SSOFC at 800 °C in wet-H<sub>2</sub>. For clarity, each step in Fig. 9a has been sequentially numbered, with the steps including galvanostatic (the current density was 0.5 A cm<sup>-2</sup> in the first 60 h and then 0.4 A cm<sup>-2</sup> for the remainder of the experiment), potentiodynamic (potential scan rate of 1 mV s<sup>-1</sup> from the OCP down to a 0.8 V cell overpotential), and OCP impedance studies (the cell was driven to the OCP condition after each galvanostatic step in order to collect the impedance data and to monitor the variations of  $R_s$  and  $R_p$ ).

An OCP value of 1.12 V, as seen in step (1), indicates that the cell was adequately sealed and that the 0.5 mm thick LSGM electrolyte

(Section 5 of Supporting information) was dense enough to prevent gas leakage. Thereafter, the OCP values tended to be transiently lower due to variations in the residual steam content in the rather large volume anode gas chamber, but eventually could be restored to ca. 1.12 V by keeping the cell at the OCP for more than 24 h, as seen in steps (5,6) and steps (10,11).

The cell initially exhibited a maximum power density of 0.3 W cm<sup>-2</sup> (Fig. 9b), which is very promising for a thick (0.5 mm) LSGM electrolyte-supported SOFC and is higher than reported previously for most perovskite-based SSOFCs [1,2,4]. Similar to the initial performance decay seen in the half cell study in wet-H<sub>2</sub> (Fig. 8b), the cell potential at 0.5 A cm<sup>-2</sup> (Fig. 9a) and the maximum power density (Fig. 9b) decreased by ca. 30% over a 25 h period. As the long-term performance of the LSCF-3 cathode was shown to be relatively stable (Fig. 4) and as the total cell performance seems to be anode rather than cathode limited (Fig. 3 vs. Fig. 8), this rapid decay can be attributed to the phase change of the LSCF-3 anode in wet-H<sub>2</sub>. This degradation behavior was also observed for cells tested at 700 °C in wet-H<sub>2</sub>, giving smaller cell potential loss rates of 2.4 mV h<sup>-1</sup> at 0.2 A cm<sup>-2</sup> over a 24 h period.

After 50 h, relatively small cell potential loss rates of ca. 1 mV h<sup>-1</sup> were observed during each galvanostatic step (Fig. 9a). However, much of this transient behavior was due to switching between polarized and unpolarized conditions and the net cell degradation from 50 to 330 h was a far more modest 0.12 mV h<sup>-1</sup>. Likewise, the decay in the power curve maximum (Fig. 9b) at 26 h (after (4)) and 325 h (after (25)) was only 0.014 mW h<sup>-1</sup>. This implies that the converted LSCF-3 phase, i.e., the LaSrFeO<sub>4</sub>-based phase and  $\alpha$ -Fe, is actually a comparatively stable anode and points toward a new type of material, having a Ruddlesden–Popper structure, which has not been previously studied as a SOFC anode. In our future work, we will determine how the  $\alpha$ -Fe phase influences the electrochemical properties of LaSrFeO<sub>4</sub>-based anodes and then modify the composition of these new composite materials to further optimize their electrochemical performance.

Because metal oxide anodes tend to be more redox tolerant than Ni cermets, the LSCF-3-based SSOFC was subjected to two redox cycles (Fig. 9a) by purging the anode chamber with air for ca. 12 h (steps (12, 25)). Based on Equation (2), the re-oxidation of the reduced anode should restore the original LSCF-3 perovskite phase, which should result in full recovery of the cell performance. However, this is not seen for our SSOFC, as only small, transient improvements are obtained in the cell performance (steps (14, 27)) relative to the initial performance (step (2)), and the power curve (Fig. 9b, taken after step (25)) showed an improvement of only ca. 20%. This implies that phase interconversion is a complex process that may have the potential to physically alter the microstructure of the anode (this is not observed by SEM, as shown in Section 5 of Supporting information) or induces cation interdiffusion at the anode/LDC and LSGM/LDC interfaces.

It is clear when comparing Figs. 3 and 8 that the SSOFC cell performance is anode rather than cathode limited. To further demonstrate this, Fig. 10a shows the typical impedance spectra of the LSCF-3-based symmetrical SSOFC obtained, as an example, during step 5 in Fig. 9a, when the composition of the anode and cathode gases was systematically changed. (Note that the impedance spectra collected at the OCP during other steps are shown in Section 7 of Supporting information). All of the spectra consist of two arcs, with the low frequency (LF) arc decreasing in size as the H<sub>2</sub> concentration increases (lower pO<sub>2</sub>) and the high frequency (HF) arc decreasing when switching the cathode gas from air to O<sub>2</sub> (using wet-H<sub>2</sub> as the fuel). These responses indicate that the LF arc is predominantly associated with the anode, while the HF arc is more cathode-related.

To determine where the long-term resistive losses are occurring, each impedance spectrum was fitted to an equivalent circuit

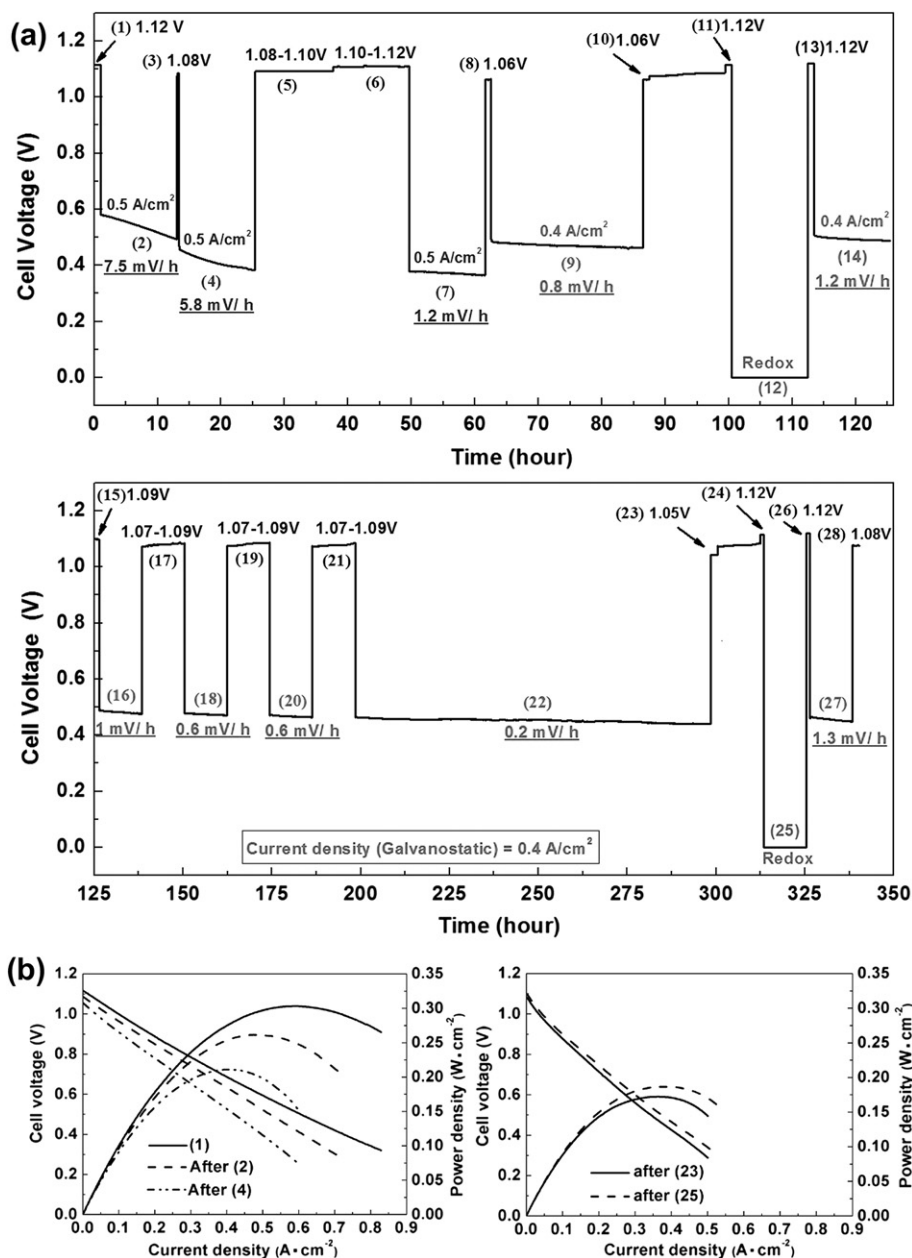


**Fig. 9.** (a) Long-term cell voltage of the LSFC-3-based SSOFC at 800 °C with wet-H<sub>2</sub> as the fuel and air as the oxidant. In the first 60 h, galvanostatic studies were conducted using a current density of 0.5 A cm<sup>-2</sup>, after which a current density of 0.4 A cm<sup>-2</sup> was used. (b) *I*–*V* and *P*–*P* plots obtained after steps (1), (2), (4), (22), and (25) in (a).

of the form:  $LR_s(R_H Q_H)(R_L Q_L)$ , where subscripts H and L refer to the high and low frequency arcs, respectively,  $L$  is an inductor,  $R$  is resistance, and  $Q$  is constant phase element.  $Q$  is represented by two variables, the capacitance ( $C$ ) and  $n$ , where  $n$  indicates the type of  $Q$  present. An  $n$  of  $\sim 1$  is a pure capacitor and when  $n$  is 0,  $Q$  is a resistor [32].

The  $R_s$  values (Fig. 10b) increase with time from 0.60 to 0.95  $\Omega$  cm<sup>2</sup> over 350 h, equivalent to a modest decay rate of 1 m $\Omega$  h<sup>-1</sup>. This may result from cation inter-diffusion between the multi-layers of the cells and subsequent decomposition of other phases unrelated to LSFC-3 (see below).  $R_L$  increases rapidly in the first 48 h, as expected (Fig. 10b). After that,  $R_L$  follows the OCP fluctuation, with a lower OCP resulting in a smaller  $R_L$  value. This behavior can also be observed by comparing the impedance spectra plots after step (5) in Fig. S8. As mentioned above, the OCP is related

to the water content generated by the cell, which directly reflects the pO<sub>2</sub> values on the anode side. Considering that the LF arc is more anode-related, it is reasonable to suggest that the fuel oxidation kinetics for the LaSrFeO<sub>4</sub> +  $\alpha$ -Fe anode improved at higher pO<sub>2</sub>. Comparatively, there is only a small increase of the cathode-related  $R_H$ , agreeing well with our previous suggestion that LSFC-3 is a stable SSOFC cathode material.

In terms of the capacitive response of the SSOFC, the  $C_L$  values (anode) are in the range of 1.5–2.5 F cm<sup>-2</sup> ( $n_L$  ca. 0.9), two order of magnitude higher than the cathode  $C_H$  values ( $n_H$  ca. 0.5) (Section 7 of Supporting information). A large capacitance in the frequency range of 0.01–1 Hz can be ascribed to the oxide chemical capacitance [33], which is related to its redox chemistry (in this case, of the Fe<sup>3+</sup>/Fe<sup>4+</sup> or Cr<sup>3+</sup>/Cr<sup>4+</sup> reactions), typical of mixed-conducting SOFC electrodes [11].

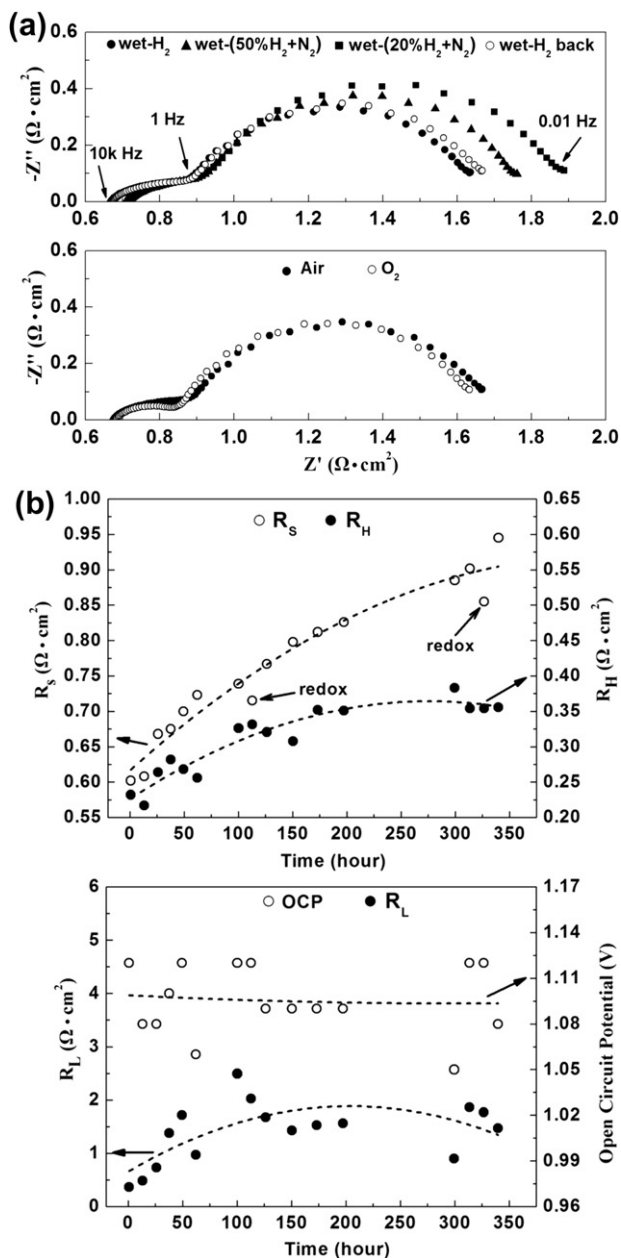


**Fig. 10.** (a) Typical impedance spectra of the LSFC-3-based SSOFC measured at step 5 in Fig. 9a when the composition of the anode and cathode gases was systematically changed. (b) Time dependence of  $R_s$ ,  $R_H$ ,  $R_L$  and the OCP, abstracted from the fitting results of the impedance spectra measured in each OCP step. The subscripts H and L refer to the high and low frequency arcs in the impedance spectra, respectively.

Hydrocarbon reformates more accurately reflect the fuel that an SSOFC would use. Therefore, studies were also carried out using the symmetrical LSFC-3-based SSOFC at 800 °C, but fueled with simulated syngas reformates (i.e.,  $H_2/CO/H_2O$  with/without ppm levels of  $H_2S$ ). Fig. 11 shows the long-term cell voltage study (at  $0.4 \text{ A cm}^{-2}$ ) under varying fuel conditions at 800 °C. In wet-(50%  $H_2 + N_2$ ), a condition that maintains the single-phase LSFC-3 perovskite, the cell underwent a slow degradation rate of  $0.8 \text{ mV h}^{-1}$  during the first 13 h (step (1)). This is comparable to the long-term stability seen in wet- $H_2$  after the first 50 h (Fig. 9a), again suggesting that long-term cell performance losses are mostly unrelated to the use of LSFC-3.

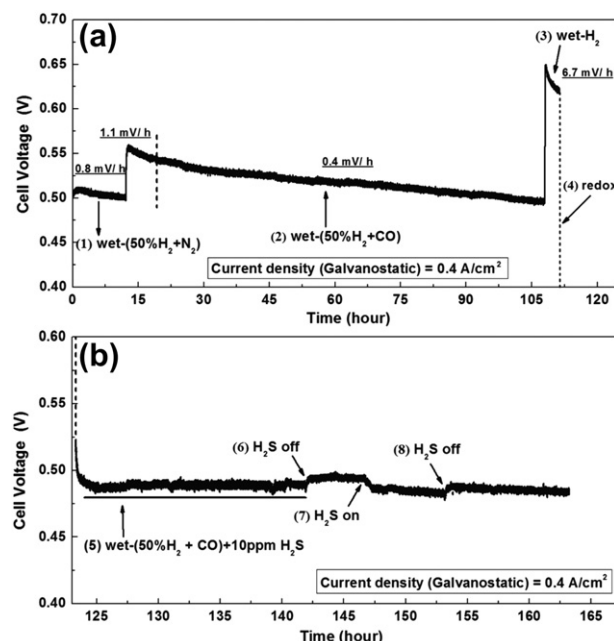


**Fig. 11.** Long-term cell voltage of the LSFC-3-based SSOFC at  $0.4 \text{ A cm}^{-2}$  and 800 °C in (a) wet-(50% $H_2 + N_2$ ), followed by wet-(50% $H_2 + CO$ ), and (b) wet-(50%  $H_2 + CO$ ) + 10 ppm  $H_2S$  (showing two cycles of the  $H_2S$  off/on process).

When the fuel was switched to wet-(50% $H_2 + CO$ ) (13–108 h, step (2), Fig. 11), the cell performance improved slightly and the losses remained as low as  $0.4 \text{ mV h}^{-1}$  rate. The introduction of wet- $H_2$  (step(3), Fig. 11) greatly increased the cell potential from 0.50 to 0.65 V, but the high degradation rate of  $6.7 \text{ mV h}^{-1}$  again shows the expected phase conversion of LSFC-3. Anode air exposure was then used to regenerate the LSFC-3 single phase (for 12 h, step (4), Fig. 11), after which wet-(50% $H_2 + CO$ ) containing 10 ppm  $H_2S$  was introduced to the anode side (steps (5,7)). As can be seen, low levels of  $H_2S$  result in only a small drop in cell potential, indicating very good stability of LSFC-3 as an anode in sulfur-containing fuels.

Throughout these studies, there was a persistent cell performance decay of roughly  $0.5 \text{ mV h}^{-1}$  (Figs. 9 and 11) that was not associated with the LSFC-3 phase interconversion within the anode. Electron probe micro-analysis (EPMA) of a polished cross-section of the cell used in Figs. 9 and 10 revealed a possible explanation for this decay. Although back scatter electron (BSE) images and individual WDX element maps in Fig. 12 show little evidence of cation inter-diffusion between adjacent cathode or anode film layers, considerable phase segregation was observed within the LSGM electrolyte immediately adjacent to the LSGM/LDC anode interface. Seen as a large  $100 \mu\text{m}$  wide defect, and a less noticeable ca.  $30 \mu\text{m}$  thick band along the anode interface in these images, these defects show considerable Ga and La segregation, possibly indicating the formation of an insulating  $LaSrGa_3O_7$  phase [34].

Because this phase segregation was not seen on the cathode side, or for half cell samples tested in wet- $H_2$  for 96 h (data not shown), this type of decomposition seems unique to cell studies run at reasonably high power densities. The same phenomenon was also reported previously when the operational inhomogeneities in  $La_{0.9}Sr_{0.1}Ga_{0.8}Mg_{0.2}O_{3-\delta}$  electrolytes and  $La_{0.8}Sr_{0.2}Cr_{0.82}Ru_{0.2}O_{3-\delta}-Ce_{0.9}Gd_{0.1}O_{2-\delta}$  composite anodes were investigated [35]. The presence of defective regions in this earlier study was explained by the combined effect of high electrical and chemical potential gradients present at the anode–electrolyte interface, which will directly impact on cell performance.

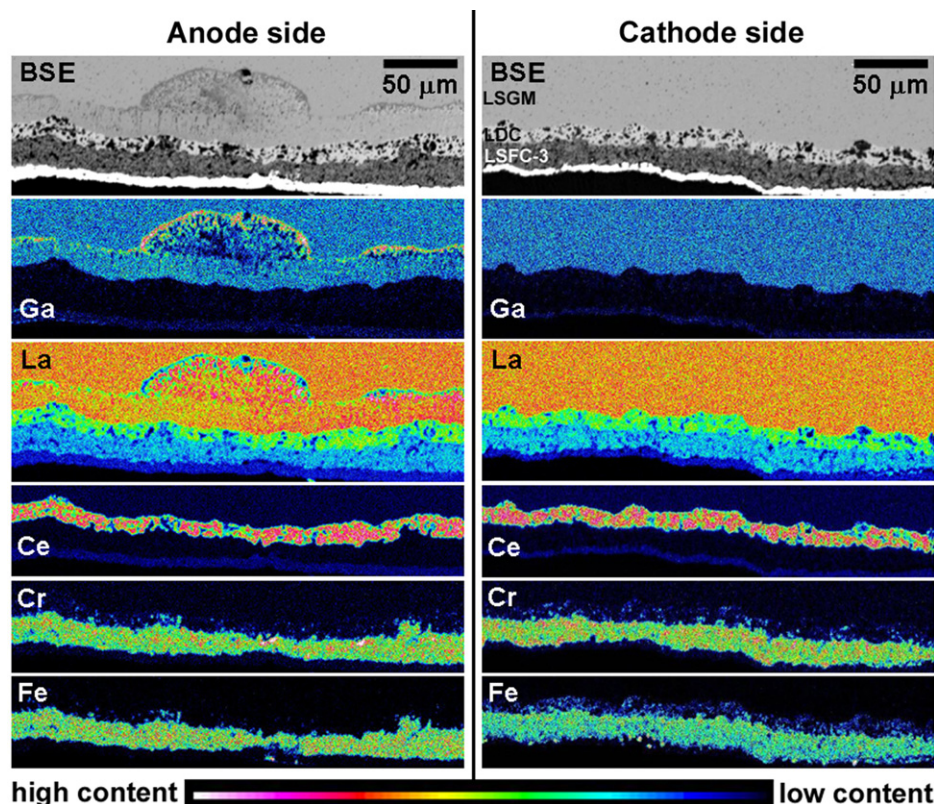


**Fig. 12.** BSE images and element maps for Ga, La, Ce, Cr and Fe at the LSGM/LDC/LSFC-3 interface at both the anode and cathode side of a LSFC-3-based SSOFC after 350 h in wet-H<sub>2</sub> at 800 °C.

#### 4. Conclusions

Cr-substituted La<sub>0.3</sub>Sr<sub>0.7</sub>FeO<sub>3-δ</sub> electrode materials with varying Cr content were investigated as electrodes for SSOFCs applications. As a cathode, the trade-off between structure, electrical conduction, thermal expansion, and electrochemical properties led to the selection of LSFC-3 as the optimum material. In a Ni-YSZ anode-supported cell, the use of LSFC-3 as the cathode gave a maximum power density of 0.63 W cm<sup>-2</sup> and a low degradation rate of 0.13 mV h<sup>-1</sup> at a constant current density of 0.75 A cm<sup>-2</sup> at 800 °C.

As an anode, Cr substitution contributes to disorder in the oxygen vacancies as well as improved structural stability of the La<sub>0.3</sub>Sr<sub>0.7</sub>FeO<sub>3-δ</sub> material in reducing atmospheres, with the LSFC-3 material showing the best structural stability of the LSFC family, down to a pO<sub>2</sub> of 1.9 × 10<sup>-21</sup> atm. Even though the LSFC-3 material decomposes at a pO<sub>2</sub> below this, such as in wet-H<sub>2</sub>, re-oxidation can restore it to the original single perovskite compound. When using wet H<sub>2</sub> as the fuel, the LSFC-3-based SSOFC exhibits a maximum power density of 0.3 W cm<sup>-2</sup> at 800 °C in the initial stage, which is very promising for a 0.5 mm LSGM electrolyte-supported SOFC.

With time, however, the LSFC-3 anode undergoes a slow structural change, forming a LaSrFeO<sub>4</sub>-based Ruddlesden–Popper phase and α-Fe in wet-H<sub>2</sub>, resulting in a drop in the cell power density by ca. 30% within 48 h, but thereafter, a still promising 0.2 W cm<sup>-2</sup> power density was maintained over several hundred hours. This re-oxidation process partially recovered the cell performance, implying the existence of some irreversible processes during long-term stability cell testing. This was suggested to be the formation of an LaSrGa<sub>3</sub>O<sub>7</sub> insulating phase, formed by cation interdiffusion at the LSGM/LDC interface under polarized conditions. The LSFC-3 anode was shown to be stable in wet-(50%H<sub>2</sub> + CO) fuel,

resulting in a relatively stable performance of the LSFC-3-based SSOFC. Importantly, only a small decrease in the cell voltage, which is fully reversible, was observed after introducing 10 ppm H<sub>2</sub>S into the wet-(50%H<sub>2</sub> + CO) fuel, indicating that LSFC-3 is a very promising anode in an H<sub>2</sub>S-containing environment.

Finally, since fuel flexibility is one of the key advantages of SOFCs, there is great interest in operating SSOFCs on hydrocarbon fuels. Although we have found that the performance of our LSFC-3-based SSOFCs was only moderate in CH<sub>4</sub> at 800 °C, we have recently discovered that it can be very significantly improved by the addition of catalytic amounts of Ni (ca. 1 wt%) into the LSFC-3 anode. This is the subject of new research currently underway in our group.

#### Acknowledgments

Grateful acknowledgments are extended to Carbon Management Canada (a Canadian National Centre of Excellence), the Institute for Sustainable Energy, Environment and Economy (ISEEE) at the University of Calgary, as well as the SOFC Canada NSERC Strategic Research Network for covering the costs associated with this work. We also extend our thanks to Jack Kan (University of Calgary) and Professor Jing-li Luo (University of Alberta) for technical assistance with the *in-situ* XRD and thermal expansion measurements, and Dr. Rob Marr (University of Calgary) for his help with the electron microprobe analyses.

#### Appendix A. Supplementary data

Supplementary data related to this article can be found at <http://dx.doi.org/10.1016/j.jpowsour.2013.02.024>.

## References

- [1] J.C. Ruiz-Morales, D. Marreo-López, J. Canales-Vázquez, J.T.S. Irvine, *RSC Adv.* 1 (2011) 1403–1414.
- [2] Y.C. Zhang, Y. Shen, X.B. Du, J.X. Li, X.J. Cao, T.M. He, *Int. J. Hydrogen Energy* 36 (2011) 3673–3680.
- [3] Q. Liu, X.H. Dong, C.X. Xiao, F. Zhao, F.L. Chen, *Adv. Mater.* 22 (2010) 5478–5482.
- [4] A. El-Himri, D. Marrero-López, J.C. Ruiz-Morales, J. Peña-Martínez, Pedro Núñez, *J. Power Sources* 188 (2009) 230–237.
- [5] G.J. Heynderickx, E.M. Schools, G.B. Marin, *Ind. Eng. Chem. Res.* 45 (2006) 7520–7529.
- [6] J. Peña-Martínez, D. Marrero-López, D. Pérez-Coll, J.C. Ruiz-Morales, *Electrochim. Acta* 52 (2007) 2950–2958.
- [7] Y. Zheng, C. Zhang, R. Ran, R. Cai, Z. Shao, D. Farrusseng, *Acta Mater.* 57 (2009) 1165–1175.
- [8] Y. Lin, C. Su, C. Huang, J.S. Kim, C. Kwak, Z. Shao, *J. Power Sources* 197 (2012) 57–64.
- [9] T. Wei, Q. Zhang, Y. Huang, J.B. Goodenough, *J. Mater. Chem.* 22 (2011) 225–231.
- [10] T. Ishihara, *Perovskite Oxide for Solid Oxide Fuel Cells*, Springer, New York, 2009, pp. 169–170.
- [11] Q.X. Fu, F. Tietz, D. Stöver, *J. Electrochem. Soc.* 153 (2006) D74–D83.
- [12] S. Tao, J.T.S. Irvine, *J. Electrochem. Soc.* 151 (2004) A252–A259.
- [13] S. Tao, J.T.S. Irvine, *Chem. Mater.* 16 (2004) 4116–4121.
- [14] I. Kaus, K. Wiik, K. Kleveland, B. Krogh, S. Aasland, *Solid State Ionics* 178 (2007) 817–826.
- [15] E. Bartonickova, K. Wiik, K. Maca, H.L. Lein, E.A. Rudberg, *J. Eur. Ceram. Soc.* 30 (2010) 605–611.
- [16] A. Ecdou, V. Zaspalis, L. Nalbandian, *Fuel* 89 (2010) 1265–1273.
- [17] V.L. Kozhevnikov, I.A. Leonidov, J.A. Bahteeva, M.V. Patrakeeve, E.B. Miterg, K.R. Poeppelmeier, *Chem. Mater.* 16 (2004) 5014–5020.
- [18] J.M. Haag, B.D. Madsen, S.A. Barnett, K.R. Poeppelmeiera, *Electrochem. Solid-State Lett.* 11 (2008) B51–B53.
- [19] I.A. Leonidov, V.L. Kozhevnikov, M.V. Patrakeeve, E.B. Miterg, K.R. Poeppelmeier, *Solid State Ionics* 144 (2001) 361–369.
- [20] L.W. Tai, M.M. Nasrallah, H.U. Anderson, D.M. Sparlin, S.R. Sehlin, *Solid State Ionics* 76 (1995) 259–271.
- [21] L.W. Tai, M.M. Nasrallah, H.U. Anderson, D.M. Sparlin, S.R. Sehlin, *Solid State Ionics* 76 (1995) 273–283.
- [22] V.V. Khaton, A.P. Viskup, E.N. Naumovich, F.M.B. Marques, *J. Mater. Chem.* 9 (1999) 2623–2629.
- [23] I. Riess, D.S. Tannhauser, *Solid State Ionics* 7 (1982) 307–315.
- [24] G.H. Jonker, *Physica* 20 (1954) 1118–1122.
- [25] V.V. Kharton, A.A. Yaremchenko, M.V. Patrakeeve, E.N. Naumovich, F.M.B. Marques, *J. Eur. Ceram. Soc.* 23 (2003) 1417–1426.
- [26] F. Tietz, *Ionics* 5 (1999) 129–139.
- [27] M. Chen, B.H. Moon, S.H. Kim, B.H. Kim, Q. Xu, B.G. Ahn, *Fuel Cells* 12 (2012) 86–96.
- [28] V. Dusastre, J.A. Kilner, *Solid State Ionics* 126 (1999) 163–174.
- [29] E. Boehm, J.M. Basset, M.C. Stil, P. Dordor, F. Mauvy, J.C. Grenier, *Solid State Sci.* 5 (2003) 973–1074.
- [30] L. Mohaddes-Ardabili, H. Zheng, S.B. Ogale, B. Hannoyer, W. Tian, J. Wang, S.E. Lofland, S.R. Shinde, T. Zhao, Y. Jia, L. Salamanca-Riba, D.G. Schlom, M. Wuttig, R. Ramesh, *Nat. Mater.* 3 (2004) 533–538.
- [31] C.Y. Park, D.X. Huang, A.J. Jacobson, L. Hu, C.A. Mims, *Solid State Ionics* 177 (2006) 2227–2233.
- [32] Q. Huang, R. Hui, B. Wang, J. Zhang, *Electrochim. Acta* 52 (2007) 8144–8164.
- [33] S.B. Adler, *Chem. Rev.* 104 (2004) 4791–4843.
- [34] K.N. Kim, B.K. Kim, J.W. Son, J. Kim, H.W. Lee, J.H. Lee, J. Moon, *Solid State Ionics* 177 (2006) 2155–2158.
- [35] Y. Liao, D.M. Bierschenk, S.A. Barnett, D. Marks, *Fuel Cells* 11 (2011) 635–641.